Journal of Catalysis 413 (2022) 252–263

Contents lists available at ScienceDirect

Journal of Catalysis

journal homepage: www.elsevier.com/locate/jcat

Proton shuttling flattens the energy landscape of nitrite catalytic reduction

Pengcheng Huang [a,1], Yu Yan [b,1], Aayan Banerjee [a], Leon Lefferts [a], Bin Wang [b,*], Jimmy A. Faria Albanese [a,*]

[a] Catalytic Processes and Materials Group, Faculty of Science and Technology, MESA+ Institute for Nanotechnology, University of Twente, PO Box 217, 7500 AE Enschede, The Netherlands
[b] School of Chemical, Biological and Materials Engineering, University of Oklahoma, Norman, OK 73019, USA

ARTICLE INFO

Article history:
Received 10 March 2022
Revised 4 June 2022
Accepted 7 June 2022
Available online 25 June 2022

Keywords:
Nitrite hydrogenation
Proton shuttling
Co-limiting reaction steps

ABSTRACT

Water molecules can enhance or inhibit hydrogenation reactions depending on the nature of the reactive species and active sites. In metal-catalyzed nitrite (NO_2^-) reduction the presence of protons is essential to complete the reaction in the aqueous phase. By coupling rigorous kinetics studies of nitrite hydrogenation on Pd with kinetic isotope studies and theoretical calculations we have shown that, contrary to previously proposed mechanisms of surface H-insertion on NO*, in aqueous environments the reaction proceeds via H-shuttling in which protons move via the aqueous environment while the electrons reach the NO* through the metal in a concerted fashion. This unique mechanism flattens the energy landscape, which leads to the same apparent activation energy barrier (0.6 eV) for the formation of HNO* and HNOH*. These results are consistent with the hydrogen reaction orders, kinetic isotopic experiments, and micro-kinetic modeling including co-limiting reaction steps for NO* hydrogenation to HNO* and HNOH*. This work provides new insights that will be key in developing more efficient catalysts and processes for catalytic removal of micro-pollutants, such as nitrate and nitrite, in drinking water and more broadly to hydrogenation reactions in aqueous phase.

1. Introduction

In nature water plays a crucial role in facilitating the operation of bio-chemical redox processes like those involved in the carbon and nitrogen cycles. For instance, in nitrogen reducing, molybdenum enzymes (NR-Mo) it has been shown that four ordered water molecules located near the metal site define the binding site of nitrates.[1]This is not surprising as proton transfer reactions, that are enhanced by hydrogen bonding provided by water, are required in the reduction of nitrate to nitrite. These N oxyanions are essential in the pathway to N_2 that closes the N-cycle. When conducting these reactions in solid catalysts these localized molecular interactions, ubiquitous to aqueous environments, cannot be captured using classical solvation theories, such as those proposed by Debye and Hückel,[2] Kirkwood,[3] and Kamlet and Taft,[4] as the continuum description cannot capture the complexity that arises at the solid–liquid interface. It is clearly the role of molecular water in the catalytic cycle what makes a detailed knowledge of these interactions essential in heterogeneous catalysts.[5,6].

Aqueous environments are often avoided in heterogeneous catalysis as water can be detrimental for the reaction due to either strong adsorption to the catalyst active sites inhibiting the rate, degradation of the support via hydrolysis, oxidation of metal clusters, or the lixiviation of the catalyst active phase. In many cases, however, water presence is unavoidable. This is the case of catalytic reduction of nitrate (NO_3^-) and nitrite (NO_2^-) in drinking water.[7–9] The reaction has gained renewed interest primarily due to the leakage of nitrogen-based fertilizers from intensive agricultural activities into natural aquifiers.[10] These contaminants can directly or indirectly cause a series of diseases in humans, such as blue baby syndrome, cancer, and hypertension, and severely damage to the environment via eutrophication of water bodies.[11] This has resulted in strict limits of these micropollutants in drinking water. According to the World Health Organization (WHO), the maximum allowable levels of nitrate, nitrite, and ammonia concentration in drinking water are 50 mg/L, 3 mg/L, and 1.5 mg/L, respectively.[12] Depending of the reaction conditions, media, and catalyst chemistry the selectivity can be steered towards nitrogen or ammonia.[13–15] The latter, however, is an undesired product as its toxicity is even higher than that of nitrite.

* Corresponding authors.
E-mail addresses: wang_cbme@ou.edu (B. Wang), j.a.fariaalbanese@utwente.nl (J.A. Faria Albanese).
[1] Equal contribution.

https://doi.org/10.1016/j.jcat.2022.06.007
0021-9517/

Considering the low concentrations of nitrates and nitrite in drinking water it is essential to use catalysts with extremely high activity and selectivity to nitrogen at near ambient conditions.[16] While the hydrogenation of nitrates to nitrite readily occurs on oxophilic Cu-based catalysts,[17,18] the reduction of the latter to dinitrogen, requires catalysts that can activate both H_2 dissociation and N-N bond formation. This is typically achieved using noble catalysts (e.g. palladium and rhodium).[17–21] Here, protons, molecular hydrogen, nitrates, and nitrite actively participate in the reaction. Specifically, protons play an essential role in this reaction. For instance, on Rh catalysts it has been shown that slow reaction kinetics are obtained in acidic pH due to the strong adsorption of NO* species on the surface, which are readily formed from HNO_2.[22] Notably, deprotonation of HNO_2 at high pH led to measurable rates and high selectivity towards ammonia. This was attributed to slower dissociation rates of NO_2^- to NO* on Rh. In contrast, on Pd very fast reaction kinetics and nearly complete selectivity to nitrogen was observed at low pH. [23,24] This trait of nitrite hydrogenation makes it a perfect reaction probe for studying the role of water on the reaction activity and selectivity of metal catalysts.

The reaction mechanism of nitrite has been extensively studied in the past using experimental,[23–31] spectroscopic,[7,32–34] and computational tools.[22,29,35–37] On Pd-based catalysts detailed spectroscopic and reaction kinetic studies have shown that NO_2^- undergoes hydrogenolysis to NO* and H_2O in the presence of protons and hydrogen. [25,26,34] This critical intermediate could either dissociate into N- and O- atoms,[27] or undergo dimerization with another NO,[28] or couple with H [22,23,25,26,34] before forming N_2. Density functional theory (DFT) calculations have shown that dissociation of N-O is kinetically unfavorable with barriers of 1.46 eV.[22] Likewise, NO* dimerization reactions are considered unlikely to occur due to the increased repulsion forces caused by the dipole–dipole interaction of chemisorbed NO*.[29] In this scenario, the H-insertion on surface NO* species seems to be the most possible pathway.

In-depth analysis of the reaction kinetics of the published literature (see Table 1) reveals that significant changes in the reaction order take place with the reactant concentration. For instance, when the concentration ranges used were relatively narrow with nitrite concentrations and hydrogen pressures of 0.1–1 mM and 0.1–1 bar, respectively, the apparent reaction orders in hydrogen varied between 0 and 0.5, while the nitrite orders ranged from 0 to 1. These observations suggest that the rate limiting step involves hydrogen insertion on surface nitrosyls species (NO* and/or HNO*). Notably, when low partial pressures of hydrogen were employed the reaction order increased to ~2, while nitrite orders became negative. This change in the hydrogen reaction order reveals that the rate limiting step drastically shifts with surface coverage to a late step in the hydrogenation mechanism.[23] These drastic changes in the rate determining step are common in electrocatalytic processes as the surface coverages can be widely varied with the applied potential. However, in low temperature thermocatalytic reactions such observations are difficult to be rationalized as surface coverages are often low. An alternative explanation could be that the apparent energy barriers for the different H-insertion steps start to reach similar values. That is that the energy landscape flattens. In this description, the degree of rate control can readily shift from different steps in the mechanism as a function of the surface coverage.

In heterogeneous catalysts water can exert multiple effects on reactivity, stability, and selectivity, including: (1) alteration of the energetics of bulk, surface, and activated complexes,[38–40] (2) participation in the reaction mechanism via H-bonding and proton transfer,[37,41,42] and (3) competitive adsorption with reactive species.[43] In this contribution, we have combined detailed catalyst characterization, catalytic measurements, kinetic isotope studies, DFT calculations, and micro-kinetics to unambiguously establish the fundamental role of water molecules in the nitrite reduction on Pd. First, we developed a set of pore-less spherical SiO_2 particles decorated with Pd clusters with well-controlled cluster size to ensure that internal mass transport limitations can be disregarded. This rigorous approach is required because selectivity in nitrite reduction appears particular sensitive to internal concentration gradients, even when catalyst efficiency is not yet affected according the Weisz-Prater criterion.[23,44] The resulting materials shows near complete selectivity to nitrogen (>99 %) and high intrinsic activity characteristic of Pd catalysts. The concerted use of catalytic testing, kinetic isotopic effects, and DFT revealed that H-insertion is facilitated by the water molecules via proton shuttling in which the electron from the H* moves via the metal, while the corresponding proton is transferred via a network of water molecules. This results in facile insertion of hydrogen on NO* and HNO* surface intermediates, explaining the change of the reaction order of hydrogen from 0 to 1.5 at high and low surface coverages, respectively. This is further illustrated using the degree of rate control of these reaction steps as a function of the hydrogen partial pressures and temperature. These new insights expand our understanding of the nitrite reduction chemistry, providing additional strategies to optimize the catalyst activity and selectivity.

2. Experimental section

2.1. Materials

Tetraethyl orthosilicate (TEOS, 98 %), ammonium hydroxide solution (NH_4OH, 25 % (NH_3 basis)), Tetraamminepalladium(II) nitrate solution ($Pd(NH_3)_4(NO_3)_2$, 10 wt% in H_2O, 99.99%), sodium hydroxide (NaOH, 99 %), methanol (99.9%) and ethanol (99.8%) were purchased from Sigma-Aldrich and used as received. All the aqueous solutions were prepared using ultra-purified water obtained on a water purification system (Millipore, Synergy).

2.2. Catalyst preparation

2.2.1. Synthesis of the SiO_2 spheres

SiO_2 spheres were prepared by the hydrolysis of TEOS in an ethanol solution in the presence of ammonia and water following the procedure originally described by Stöber et al.[47] The procedure can be summaried as follows. Firstly, two solutions were prepared. For the solution, 15 mL of TEOS dissolved in 200 mL of ethanol in an oven-dried beaker. For solution II, 50 mL of NH_4OH, 30 mL of water and 100 mL of ethanol were added. After that, the solution I was added to solution II and the reaction was allowed to proceed for 22 h at room temperature under continuous stirring (400 rpm). Then, the SiO_2 spheres were rinsed with ethanol twice. After that, the particles were dried in a vacuum oven at 50 °C overnight.

2.2.2. Synthesis of Pd/SiO_2 catalyst

Pd/SiO_2 catalyst was prepared by a strong electrostatic adsorption (SEA) method.[48,49] First, the point of zero charges (PZC) of the synthesized SiO_2 spheres was investigated (Fig. S1). The PZC of the synthesized SiO_2 is 2.3. Then, 2 g of SiO_2 were dispersed in 60 mL of deionized water via sonication for 5 min. The pH of the solution was adjusted to 10.5 by adding $NH_3{\cdot}H_2O$ solution. After that, 1.12 g $Pd(NH_3)_4(NO_3)_2$ was added dropwise to the SiO_2 dispersion, and the reaction took place for 1 h at room temperature under continuous stirring (300 rpm). During the adsorption process, the pH was kept constant at 10.5 by adding the $NH_3{\cdot}H_2O$

Table 1
Kinetics of nitrite hydrogenation at room temperature reported in the literature.

Catalyst	Reactor	pH	Hydrogen pressure (bar)	Nitrite concentration (mM)	Hydrogen order	Nitrite order
Pd/Al_2O_3 [21]	Membrane	7	0.01–1	0.24–2.4	0	N/A
$Pd/\gamma\text{-}Al_2O_3$ [30]	Slurry	4.7	0.11–1	0.11–0.65	0–0.5	0–1
Pd/Al_2O_3 [23]	Batch	5.5	0.01–0.8	0.3–10	0.3–2.3	−1–0.4
Pd/CNF [45]	Membrane	7	0.2–1	0.044–0.22	<0	N/A
Pd/AC [44]	Fixed bed	4.5–9	0.3–0.7	0.27–0.45	0.4	0.7
Pd/ACC [46]	Slurry	4.5–8	1.8–6.4	1.63	0	1

solution. The resulting solution was filtered via sequential vacuum and filtration membranes. Then, the sample was dried in a vacuum oven at 40 °C overnight. Finally, the samples were calcined at 300 °C in the air for 0.5 h and reduced in H_2 for 3 h with a heating rate of 2 °C /min.

2.2.3. Catalyst characterization

Brunauer–Emmett–Teller (BET) surface area analysis was conducted using a Micromeritics Model ASAP 2400 instrument. For each study, 0.2–0.3 g of sample was degassed at 120 °C for 24 h before measurement. The transmission electron microscopy (TEM) analysis results were obtained using a Tecnai F30 field emission TEM, with an acceleration voltage of 300KV and coupled with a HAADF detector (Fischione). The Scanning Electron Microscopy (SEM) was conducted to investigate the particle size by using a JEOL, LA6010 with a resolution of 4 nm @ 20 kV. The metal loading of the Pd/SiO_2 samples were determined by X-ray fluorescence (XRF) (Bruker, S8 TIGER). The metal dispersion of the Pd/SiO_2 samples was determined by CO chemisorption at room temperature (Micromeritics, Chemisorb 2750). The samples were reduced in H_2 at room temperature for 1 h and then flushed in He for 30 min. After that, CO was introduced as pulses, and the response was recorded using a TCD detector.

2.3. Catalytic tests

The reaction was conducted using the previously reported setup from our group.[23] Catalytic activity and selectivity were measured at atmospheric pressure with a temperature range from 25 to 50 °C. A pH value of 5.5 is maintained by buffering continuously CO_2 at a pressure of 0.1 bar. The glass reactor (DURAN ® baffled wide mouth bottle GLS 80) has four connections on the lid used for gas-in, gas-out, thermometer and sampling with a capacity of 1 L. The reaction conditions are summarized in Table S2. For a standard experiment, 0.05 g catalyst was suspended in 0.3 L deionized (DI) water and stirred at 500 rpm under 0.8 bar hydrogen (0.1 bar CO_2, 0.1 bar He) for at least 1 h, removing dissolved oxygen and reducing the catalyst. After that, the hydrogen pressure is switched to the value of choice. The reaction was started by introducing of 3 mL $NaNO_2$ solution (100 mM) in the glass reactor. Hydrogen pressure was varied between 0.01 and 0.9 bar, and the nitrite concentration was varied between 0.5 and 5 mM. The reaction temperature is controlled by an IKA contact thermometer ETS-D5. During the catalytic reaction, the samples were collected using a 5 mL syringe (BD Plastipak) and filtered with a syringe filter (PTFE 0.2 μm, Whatman). The nitrite and ammonium concentrations were explicitly analyzed using a ion-chromatography (DIONEX, ICS 3000) equipped with an autosampler and a channel for anions and cations separately for simultaneous measurement.

The apparent reaction orders and activation barriers were determined in a broad range of nitrite concentrations (0.5–5 mM), hydrogen partial pressures (0.01–0.9 bar), and temperatures (25–50 °C), using the initial rate calculated from the slope of the nitrite concentration profile as a function of time. By considering exclusively data at conversion lower than 10% it was possible to avoid the concentration effects on the rate characteristic of batch reactor operation (Fig. S4). For the activation energy investigation, the decrease of hydrogenation concentration in the solution caused by increasing the temperature is compensated by increasing the partial hydrogenation pressure according to Henry's Law. The Kinetic Isotope Effect (KIE) test was conducted by using ^{15}N-labeled $NaNO_2$ to replace the unlabeled $NaNO_2$ to investigate the influence of nitrogen atoms and by using D_2/D_2O to replace H_2/H_2O to examine the impact of hydrogen atoms. The nitrite conversion and ammonium selectivity were calculated according to Eq. (1) and eq. (2). Since nitrogen and ammonia are the only products,[23] thus the nitrogen selectivity was calculated based on the mass balance.

$$NO_2^- \text{conversion}_{t1} = \frac{[NO_2^-]_{t0} - [NO_2^-]_{t1}}{[NO_2^-]_{t0}} * 100 \quad (1)$$

$$NH_4^+ \text{selectivity}_{t1} = \frac{[NH_4^+]_{t1}}{[NO_2^-]_{t0} - [NO_2^-]_{t1}} * 100 \quad (2)$$

Here, $[NO_2^-]_{t0}$ is initial nitrite concentration, $[NO_2^-]_{t1}$ is the concentration of nitrite at t1,.$[NH_4^+]_{t1}$

2.4. Computational methodology

The calculations were carried out using periodic plane-wave DFT implemented in VASP.[50–52] The Perdew-Burke-Ernzerhof (PBE) functional within the generalized gradient approximation (GGA)[53] was used for the exchange–correlation energy. Electron-ion interactions was described by the projector augmented wave (PAW) approach, and van der Waals (vdW) interactions[54] were included using the DFT-D3 method.[55] All electronic energies in calculations were converged within 10^{-5} eV, and the force on each atom was converged to below 0.02 eV $Å^{-1}$. The simulated Pd bulk has lattice constant of 3.89 Å which is in agreement with measured crystallographic properties of Pd. The Pd (1 1 1) facet was optimized and used to build a close-packed 3x3 Pd(1 1 1) surface with thickness of 4 layers and a vacuum layer of 15 Å along z direction as the previous research [56]. The supercell as a lattice of about 1 nm, which is long enough to avoid the interaction from periodic surface. The 3 × 3 × 1 Monkhorst-pack k-point mesh was used to sample the first Brillouin zone during structural optimization. In calculations, two NO adsorbates were positioned on the Pd surface, equaling to 2/9 surface coverage. Two different solvation models were compared. The implicit solvation effect was computed by VASPsol.[57] The explicit model was investigated by incorporating different numbers of water molecule near the NO molecules and the most stable local configuration was used for activation barrier calculations. Total energies of several initial geometries of explicit water were compared(**Fig. S 8-g**), and the most stable one was adopted for calculations of activation barriers and transition states. The transition state searches were performed using the dimer method[58] with the initial guesses obtained through the nudged elastic band (NEB) method.[58,59] The transition states were further confirmed

by calculating the vibrational frequencies. The adsorption energy E_{ads} was calculated by Eq. (3).

$$E_{ads} = \frac{(E_{slab-ads} - E_{slab} - nE_{ads-gas})}{n} \quad (3)$$

Where $E_{slab-ads}$, E_{slab}, and $E_{ads-gas}$ are the total energy of adsorbate/slab system, clean metal slab, and the isolated adsorbate in gas phase, respectively, and n is the number of adsorbates in the calculations. The adsorption free energy of liquid-phase NO_2^- on Pd surface was obtained by thermodynamic cycle discussed in SI section 5.1. For hydrogen adsorption calculations, the residual H entropy upon adsorption was assumed to be the value reported for adsorption of H over Pd black.[60] The discussion on H entropy is covered and shown in Fig. S6 and section 5.2 in SI. Also in SI, section 5.4 and 5.5 validate the micro-solvation model (1,2,3 water molecules) and investigate the entropy and enthalpy contribution on activation free energies as well as loss of water entropy in the proposed mechanism.

2.5. Data reconciliation and parameter estimation

The kinetic model was evaluated by determining the parameter values that minimize the objective function given in Eq. (4).[61].

$$SSE = \sum_{i=1}^{n} (\log_{10}(TOF_{EXP_i}) - \log_{10}(TOF_{MOD_i}))^2 \quad (4)$$

The square error for any experiment ***i*** was obtained by the difference between measured Turnover Frequency (TOF) and the corresponding model prediction at the same condition. The residual sum of squares (SSE) was combined with the total sum of squares (SST, Eq. (5)) to obtain the determination coefficient (R^2, Eq. (6)) and the Akaike Information Criterion (AIC, Eq. (7)) for each least squares solution.[62] Especially, the AIC involves a regression for variable parameter numbers, which helps identify the overfitting case and determine a statistically preferred model.

$$SST = \sum_{i=1}^{n} (\log_{10}(TOF_{EXP_i}) - \frac{1}{n}\sum_{i=1}^{n} \log_{10}(TOF_{EXP_i}))^2 \quad (5)$$

$$R^2 = 1 - \frac{SSE}{SST} \quad (6)$$

$$AIC = 2n_k + \ln(SSE) \quad (7)$$

In equations (5)-(7), *n* is the experimental measurements numbers and n_k is the number of adjustable parameters regressed in a model.

3. Result and discussion

3.1. Nitrite hydrogenation over Pd/SiO_2 catalyst

3.1.1. Catalyst structure

The catalysts were characterized using SEM, HR-TEM, N_2 adsorption, and CO chemisorption (Table 2). The SEM image shows that the synthesized silica support has a diameter of ~500 nm (Fig. S2). The specific surface area of SiO_2 and Pd/SiO_2 shows a very similar value, suggesting that the structure and porosity of the support remained unaltered after metal deposition. In addition, the value is very close to that theoretically estimated for a non-porous spherical silica particle with a diameter of 500 nm (Table 2). TEM characterization shows an average metal particle size of 2.5 nm (Fig. S3), which agrees with the average particle size regressed from CO-chemisorption measurements.

3.1.2. Mass transfer effects

To discern mechanistic information we conducted rigorous analysis of role of mass transfer effects on the experimentally measured rates. Heat transport limitations were assumed to be negligible due to the high heat capacity of water (4.2 kJ kg^{-1} K^{-1}), low conversion levels employed, and diluted nitrite concentrations (0.5–5 mM). Internal diffusional limitations were negligible in this Pd/SiO_2 catalyst since the specific surface area of the silica support is very close to the theoretical specific surface area of a non-porous material (i.e. sphere of 500 nm). The external mass transport limitations were assessed by measuring the turnover frequency (TOF) as a function of the agitation rate in the baffled reactor (Fig. S5), increasing the agitation to 250 rpm plateaued the TOF, indicating that external mass transfer limitations can be excluded at the conditions hereto employed. These results agree with the estimated mass transport rates for the reactants. For instance, when the nitrite concentration is 1 mM, the calculated mass transfer rate is 4.3×10^2 mM min^{-1}, which is five orders of magnitude larger than the highest reaction rate measured (5.0×10^{-3} mM min^{-1}) at the same nitrite concentration. Likewise, the Mears criterion shows that external transport of hydrogen in the G-L and/or L-S interface does not limit our measurements (Section 4.1.2 and 4.1.3 in SI). Considering that the system is free of mass transfer effects one could use the information from the apparent reaction orders to extract mechanistic insights.

3.1.3. Apparent reaction orders and activation energy

As shown in Fig. 1d the apparent activation energy barrier for the nitrite reduction in aqueous phase was 29 ± 1 kJ mol^{-1}, which is within the range reported in the literature for Pd catalysts operating at similar reaction conditions (22.6 to 35.3 kJ mol^{-1}).[24,44,63] Next, we studied the reaction orders for nitrite and hydrogen in a broad window of concentrations at low and high temperature, the overall reaction order is summarized in Table 3. The reaction order investigation presented in Fig. 1a and 1b, indicates that regardless of the reaction temperature (25 °C and 50 °C) the nitrite apparent reaction orders varied from 0.7 to 0 at high hydrogen partial pressures (0.8 bar). Notably, reducing the partial pressure of hydrogen to 0.05 bar drastically changed the reaction order to −0.9 and −0.2 at 25 °C and 50 °C, respectively. Here, the large reaction orders observed at the high hydrogen partial pressures would be consistent with the molecular chemisorption of nitrite, while the strong inhibition of nitrite observed at low hydrogen partial pressures reveals that hydrogen and nitrite compete for the same active site on the Pd surface. In contrast to previously proposed mechanisms summarized by Rosca et al.[64] who claim the N-O bond breaking is the rate-determining and hydrogenation happens on the dissociated fragments, the results herein obtained would suggest that the RDS only requires one surface N-containing surface specie as the highest apparent reaction order is significantly lower than 2 even at the low nitrite concentration region. These observations are not unique to this Pd/SiO_2 catalyst. For instance, Xu et al.[23] obtained a nitrite reaction order of −1, at low hydrogen partial pressures, when studying the hydrogenation of nitrite on Pd catalysts supported on alumina at 25 °C in a similar buffered reaction system.

In the case of hydrogen, the reaction orders varied between 1.4 and 1.2 at low partial pressures when the experiments were conducted at 25 °C and 50 °C, respectively (Fig. 1c). Above 0.1 bar the reaction reaches an asymptotic behavior characteristic of saturation kinetics regardless of the temperature employed. While the modest decrease of the reaction orders with increasing temperature could be explained in terms of the entropic contributions to the Gibbs free energy of adsorption ($\Delta G_{ads} = \Delta H_{ads} - T\Delta S_{ads}$) that effectively reduced the inhibition of the reaction rate caused by surface coverage, the significant changes of reaction orders of

Table 2
Characterization data of Pd/SiO_2 and support material SiO_2.

Sample	TEM	XRF	CO-chemisorption	N_2-physisorption		
	Pd particle size (nm)	Pd loading (wt. %)	Pd dispersion (%)	Specific surface area (m^2/g)	Theoretical specific surface area (m^2/g)	Pore volume (cm^3/g)
SiO_2	–	–	–	7.5	6.4	0.002
Pd/SiO_2	2.5	0.2	55.5	7.9	6.7	0.002

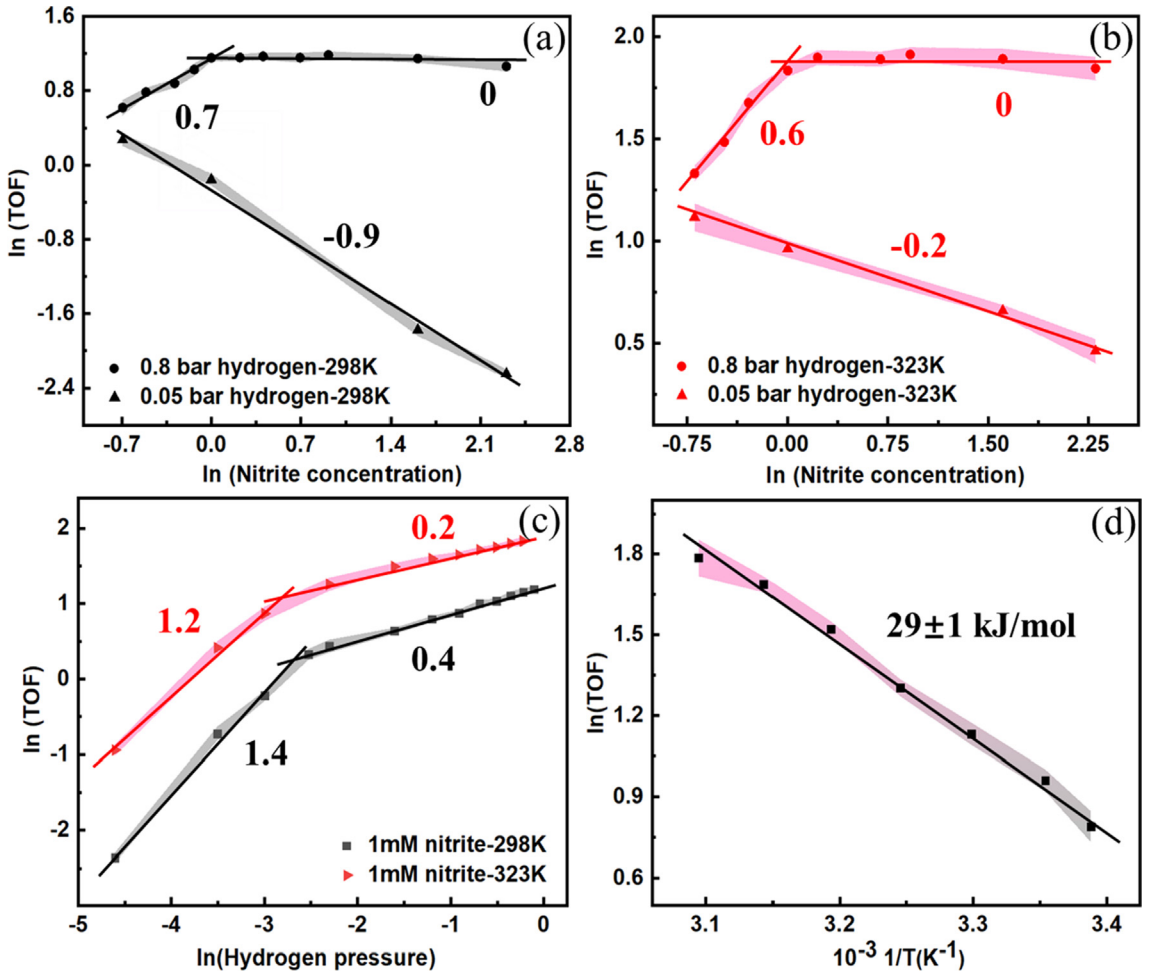

Fig. 1. (a) and (b) effect of nitrite concentration on reaction rate for 0.05 and 0.8 bar hydrogen pressure at 25 °C and 50 °C. (c) Effect of hydrogen pressure on reaction rate for 1 mM nitrite concentration at 25 °C and 50 °C, (d) Temperature dependence of turnover frequency (TOF) over temperature. The shadow shows the error margin.

Table 3
Overview of the apparent reaction orders in nitrite and hydrogen information in all ranges of the nitrite and hydrogen concentrations.

Temperature (°C)	Low hydrogen pressure		High hydrogen pressure	
	Hydrogen order	Nitrite order	Hydrogen order	Nitrite order
25	1.4 ± 0.1	−0.9 ± 0.1	0.4 ± 0.1	0.7 ± 0.1
50	1.2 ± 0.1	−0.2 ± 0.1	0.2 ± 0.1	0.6 ± 0.1

hydrogen from 1.5 to close to 0 are more difficult to rationalize. Here, one could argue these high reaction orders are associated to a late rate-determining step in which multiple pre-equilibrated hydrogenation reactions are needed before reaching the RDS. This postulate was previously proposed by Xu et al.[23] during the hydrogenation of nitrite in buffered systems over Pd/Al_2O_3. In that case, the authors obtained reaction orders for hydrogen that varied from 0.3 to 2 at 20 °C. This considerable variation was attributed to the changes in the surface coverage assuming that the rate-determining step is fixed regardless of the partial pressure of hydrogen and nitrite concentration. In this rationale, it is assumed that NO* is readily formed on the Pd surface at the pH employed in this reaction (pH ~ 5.5), which is stepwise hydrogenated to (H)NO* and $(H)_2NO^*$ before reaching the RDS involving the decomposition of $(H)_2NO^*$. An alternative proposition is that these changes are caused by a switch in the degree of rate control

of two consecutive rate-determining steps. In this scenario, at low hydrogen partial pressures the mechanism is controlled by the hydrogenation of partly hydrogenated nitro-species, e.g. (H)NO*, leading to high reaction orders, which upon increasing the pressure shifts to the preceding step in the sequence (e.g. NO* hydrogenation) with the concomitant decrease in the reaction order. To further evaluate the aforementioned postulate we conducted kinetic isotope labelling experiments.

3.1.4. ^{15}N-labelling experiments

In these experiments, the nitrogen in $NaNO_2$ was isotopically labelled with ^{15}N while all the reaction conditions were kept constant. The observed turnover frequency (TOF = 2.58 min^{-1}) for the reduction was similar to that of unlabeled $NaNO_2$ reduction (TOF = 2.68 min^{-1}). The resulting kinetic isotope effect (k_{N14}/k_{N15}) was 1.04 ± 0.02 (Table 4), which is in line with previous reports on reduction of nitrite containing aromatic molecules.[45] Considering that the maximum ratio of specific rate constants for ^{14}N to ^{15}N is 1.14 at 25 °C,[65] it is clear that the small values obtained here suggest that there is no significant primary KIE. This further supports the idea that the rate determining step is not related to N-N bond formation nor N-O cleavage as previously suggested.[64].

3.1.5. Hydrogen-Deuterium isotope effect

By conducting kinetic experiments using deuterated hydrogen and water we explored the role of hydrogen insertion in the nitrite hydrogenation. Here, we obtained primary kinetic isotope effect with a K_H/K_D value of 2.4 at 25 °C. When increasing the temperature to 50 °C, the isotope effect of K_H/K_D is 1.5 (Table 4), which is consistent with the literature that deuterium reacts less readily than hydrogen at room temperature, thus increasing the temperature the value reaches of $\sqrt{2}$.[66] From the kinetic isotope effect, it is clear that the hydrogen atom is involved in the rate-determining step.

Table 4
Kinetic isotope effect.

	KIE(K_H/K_D)[1] 25℃	KIE(K_H/K_D) [1] 50℃	KIE(K_N^{14}/K_N^{15}) [2] 25℃
Pd/SiO_2	2.37 ± 0.1	1.51 ± 0.1	1.04 ± 0.02

Note: 1. using D_2/D_2O to replace H_2 and H_2O. 2.using $Na^{15}NO_2$ to replace $Na^{14}NO_2$.

3.1.6. Effect of the hydrogen pressure, nitrite concentration and kinetic isotope effect on ammonium selectivity

The selectivity to ammonium increased with the hydrogen pressure (Fig. 2a), especially when the reaction was conducted at high temperature. This is in agreement previous work that reported higher ammonia formation as H_2 pressure and temperature increased when using a Pd/Al_2O_3 catalyst.[31] In contrast, the nitrite concentration decreased the selectivity to ammonium (Fig. 2b).[23] Experimental data on ammonia selectivity have a larger error margin, especially in the case of low hydrogen pressure and nitrite concentration. This is caused by the fact that ammonia concentration is relatively low at the beginning of the reaction, especially with a low concentration of reactant, increasing the experimental scattering.

The kinetic isotope effect results revealed that, within the experimental error, the ammonium selectivity remained unaltered upon switching to the isotopically labelled hydrogen and water (see Table S1). The same observations were obtained when N^{14} was replaced by N^{15}. This suggests that the rate determining step is before the N-N and N-H bond formation that leads to either nitrogen and ammonia, respectively.

3.2. DFT calculations

3.2.1. Nitrite reduction mechanism on a clean Pd surface

As previously mentioned, many reaction mechanisms have been proposed for nitrite reduction in aqueous solutions using Pd-based catalysts.[29,63,67–71] These reaction mechanisms commonly start with nitrite adsorption and dissociative adsorption of hydrogen to form H*, followed by hydrogenation of nitrite to form adsorbed NO*, which has been claimed as a crucial intermediate.[68,72,73] The N–O bond could dissociate directly to form N* and O*[26,27,68,74] or assisted by hydrogen via hydrolysis of HNO*, NOH* and HNOH* species. The NO* direct dissociation is hindered by its high activation barrier on Pd(1 1 1).[35] Instead, NO* hydrogenation is favored. The N-O dissociation barrier in HNO*, NOH*, and HNOH* were calculated to be higher than those of the sequential hydrogenation steps.[36] Therefore, in the following DFT calculations, we follow the hydrogenation of NO* to form NHOH, hydrolysis of which produces NH*, another surface dominant specie. The N-N bond could form between NH* and another surface species to form N_2. Instead, NH* can also proceed with

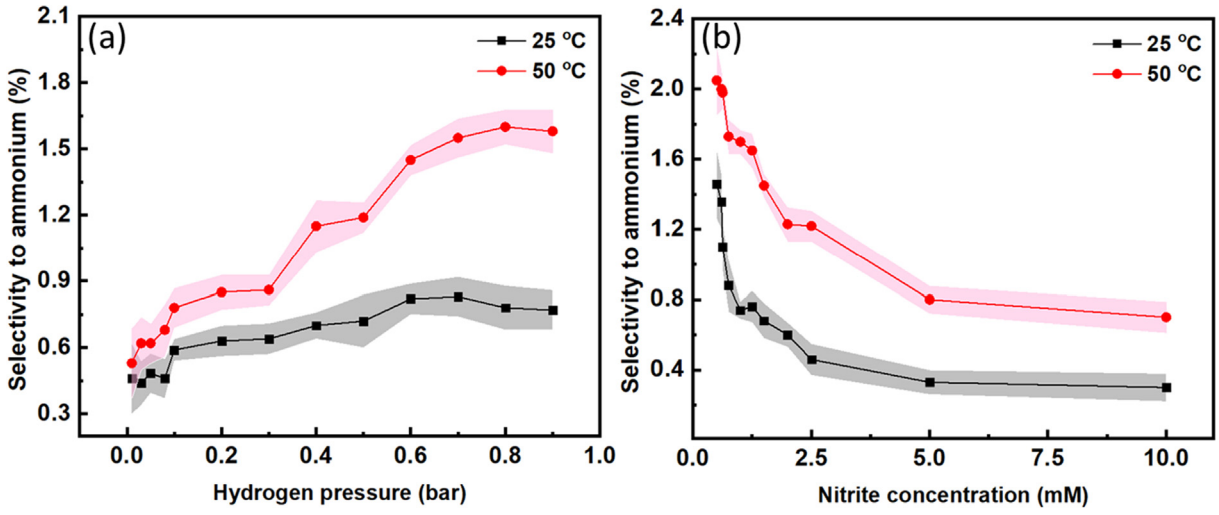

Fig. 2. (a) Selectivity to ammonium at 10 % nitrite conversion as a function of (a) hydrogen pressure, with 1 mM nitrite concentration and (b) nitrite concentration, with 0.8 bar hydrogen pressure.

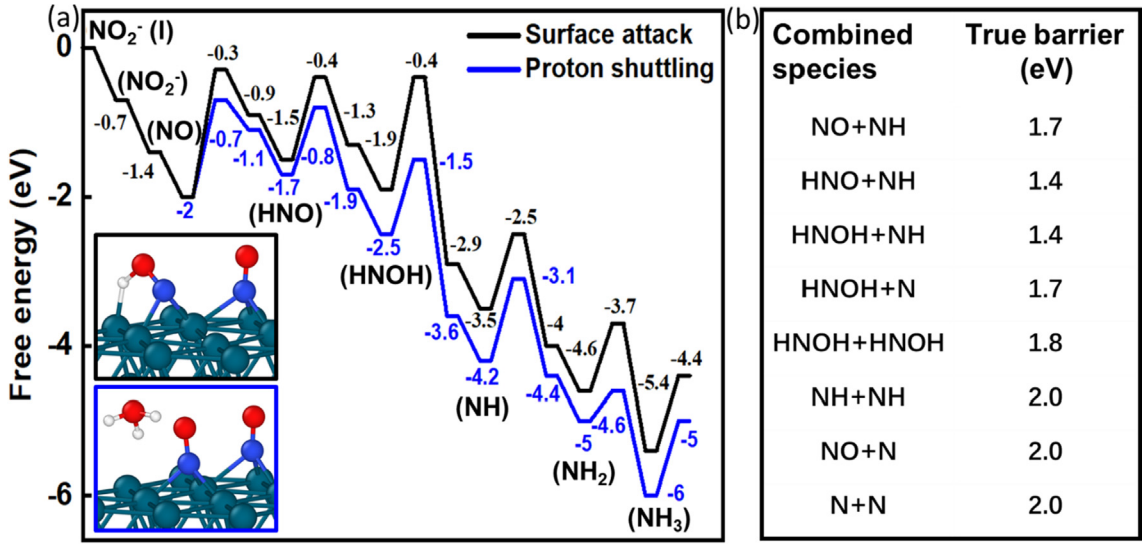

Fig. 3. (a) Free energy diagram of NO_2^- reduction on a Pd(1 1 1) surface. Black line: hydrogen directly attacks surface species. Blue line: proton shuttle through H_2O to the surface species illustrated as solvent effect in Fig. S7. The atomic structures of transition state for the first hydrogenation reaction with and without proton shuttling are shown as insets. (b)The true barriers for possible N-N coupling species. The H adsorption requires H-insertion with a free energy of c.a. 0.6 eV. (For interpretation of the references to colour in this figure legend, the reader is referred to the web version of this article.)

two more hydrogenation steps to form NH_3. The free energy profile is plotted in Fig. 3.

The adsorption energy of NO_2^- from liquid phase onto the Pd surface is – 0.7 eV, and its conversion to form NO* is exothermic by 0.6 eV. It suggests the NO_2^- favors the adsorption on Pd surface and converts to NO easily, agreeing with a previous report[29]. NO* adsorbs strongly on Pd with an adsorption energy of −2.8 eV, much stronger than hydrogen adsorption (-0.6 eV). This energy difference between NO* and H* suggests NO* likely covers the Pd surface and competes for sites, in line with the experimentally measured negative reaction order in nitrite at low hydrogen pressures. The first hydrogenation can happen at either the N or O in NO*. Our results shows the formation of NOH* is slightly favorable than HNO* (see comparison in Fig. 3). However, the kinetic barrier of HNO* toward HNOH* is feasible by difference of 0.7 eV comparing to the barrier of NOH*. Thus, Fig. 3 shows the most favorable pathway following the sequence of NO*, HNO*, HNOH*, NH* and NH_2*. Among all the elementary steps, the transition states (TS) of the first, second, and third steps to form HNO, HNOH and NH have a similar energy with the highest values. The RDS should thus be within the first three steps. Given the polar nature of the surface species the transition state energy of these steps will be very sensitive to the presence of water molecules via so-called "*solvation effects*".

3.2.2. Solvent effects on the hydrogenation and hydrogenolysis

We consider the solvent effect in two approaches: an implicit model, which includes the effect of electrostatics, cavitation, and dispersion on the interaction between a solute and reactant. Another one is the explicit model, where the actual H_2O molecules are included in the calculations. Fig. S7 shows the free energy profile of NO* hydrogenation towards HNOH* using either the implicit model or the explicit model. Here, one could notice that a similar change in the free energy of the TS and chemisorbed species has been observed for the steps of NO and HNO hydrogenation in two solvent models. In the following section, we focus on the explicit solvent model to include the proton shuttling mechanism where explicit water needs to be present to participate in the reaction. Strikingly, the results indicate that the proton shuttling has a pronounced effect in promoting the first three hydrogenation/hydrogenolysis steps, i.e. lowering their intrinsic activation barriers by 0.4, 0.2, and 0.5 eV, respectively (Fig. 3). Such an enhancement is because H_2O shortens the hydrogenation path, reducing the energy of the TS by stabilizing the positive charge at H_3O^+ (see Fig. S8). As a result, this shuttling mechanism lowers the apparent barriers. This flattening of the energy landscape leads to similar barriers for the first two hydrogenation steps.

The proton shuttling path was investigated with extra water molecules to test the convergence of the explicit model (see Fig. 4). The results with more than one H_2O molecule shows a comparable stabilization of the TS, very similar to the model with one water molecule, suggesting that the key chemistry required in this model has been captured with just one water in the proximity (Fig. S9). The true barriers for each hydrogenation, listed in Fig. 4, shows the most pronounced water promotion on the NOH* formation. When the O atom in NO* is targeted for hydrogenation, the true barrier of shuttling is reduced by 1.0 eV, almost independent on the number of water molecules. NO* adsorbs on Pd with N, leaving the O interfacing with the solvent. The H_2O molecules open a favorable shuttling path for the surface hydrogen to attack O as observed in other hydrogenation of oxygenates.[37] Yet, such a promotion effect is strictly limited for hydrogenation of O in HNO*, because in the tilted configuration of HNO*, the hydrogenation path from the surface is already shortened and facilitated. Different from the O hydrogenation, hydrogenation of N in NO* is promoted moderately by 0.5 eV, because of the extra energy cost for water to approach the surface and hydrogenate the N that is strongly bonded with Pd. A similar effect is shown for hydrogenating N in NOH*; the water enhancement for hydrogenating N in NOH* is minor. While these results might indicate that H-insertion on the O of NO* should be the most preferable pathway in the explicit water model (red curve in Fig. 4a i-iv), the barriers obtained for this mechanism are significantly larger than those obtained in the H-NO* pathway. Furthermore, the hydrogen addition to the O of NO* would result in reaction orders for hydrogen that vary between 1 and 1.5. That is, 1.5 hydrogen insertions have occurred on the system before the RDS. Such mechanism, however, would not explain the low reaction orders in hydrogen herein observed (Fig. 1c). Instead, it is more likely that hydrogen is inserted at the nitrogen atom of NO* leading to similar apparent

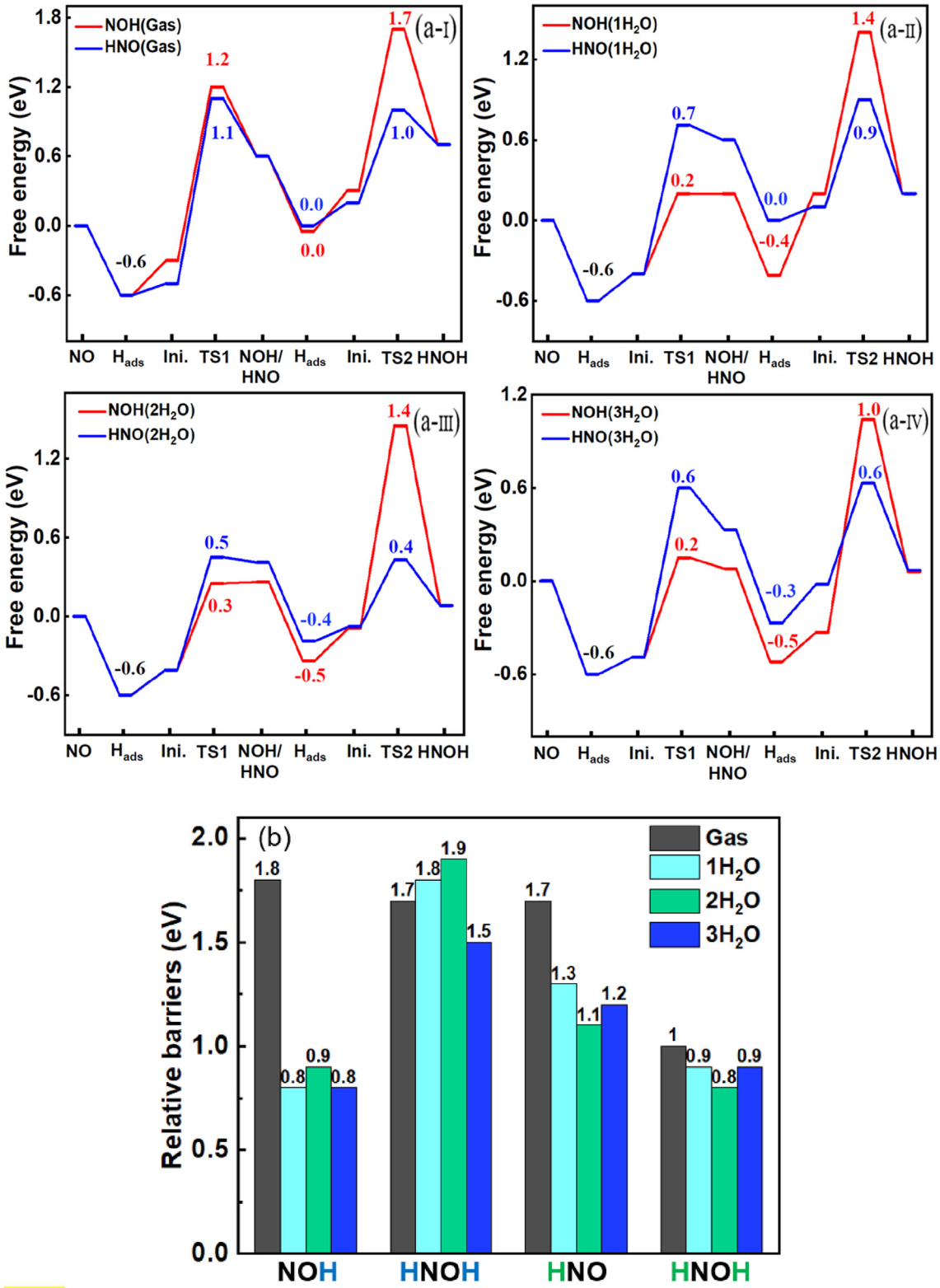

Fig. 4. Free energy diagram for NO reduction on the Pd(1 1 1) surface assisted by water in different clusters (a-Ⅰ) Gas; (a-Ⅱ) 1 H_2O; (a-III) $2H_2O$; (a-Ⅳ) $3H_2O$.(b) The relative barriers of each hydrogenation step via NOH to HNOH or via HNO to HNOH.

barriers in the two subsequent hydrogenation steps, resulting in two co-limiting rate limiting steps with reaction orders varying from 0 to 1.5 (blue curve in Fig. 4a i-iv).

It is worth noting that the reactions mediated by different number of water at the interface may require disruption of hydrogen bonds and displacing water molecules from the bulk to the interface, which can add an additional free energy change. We thus quantitively estimate the free energy change of water reconstruction (e.g., move a cluster of water (1–3 molecules) from the bulk to the interface) at room temperature (section 5.4 in SI). The

enthalpy and entropy change result from breaking hydrogen bonds between the water clusters and the water bulk during the reconstruction. Previous studies showed that such disruption of hydrogen bonds could lead to a noticeable free energy cost (~1 kJ/mol per hydrogen bond), which includes the enthalpy loss and entropy gain by breaking one hydrogen bond[75,76,77]. Such a free energy cost associated with large water clusters at the interface was also discussed in olefin epoxidation, though the exact entropy change is different as in the latter case water is partitioned from organic nitrile rather than bulk water[78]. Formation of large water clusters at the interface, which requires breaking multiple hydrogen bonds, is thus less likely than the model with one interfacial water molecule.

3. $NO_2^{-*} + H^* + H^+ \rightleftharpoons NO^* + H_2O + *$ (barrierless NO^* formation, $\boldsymbol{K}_3$)
4. $NO^* + H^* \rightarrow HNO^* + *$ (hydrogenation of NO^*, $\boldsymbol{k}_4$) **TS1** ***RDS***
5. $HNO^* + H^* \rightarrow HNOH^* + *$ (hydrogenation of HNO^*, $\boldsymbol{k}_5$) **TS2** ***RDS***
6. $HNOH^* + H^* \rightleftharpoons HN^* + H_2O + *$ (hydrogenation of $HNOH^*$, $\boldsymbol{k}_6$) **TS3**

The underlaying assumption in this mechanism is that protons are readily available in this system and that chemisorbed hydrogen on Pd is required to provide the electrons for the reduction reactions. As a result, hydrogen atoms have been included in the site balance equation. This results in the following rate expression (Eq. (8)).

$$r_{NO_2^-} = \frac{k_5 k_4 * {K_1}^{3/2} K_2 K_3 [H_2]^{3/2} [NO_2^-][H^+]}{\left[k_{-4} + k_5 K_1^{\frac{1}{2}} [H_2]^{\frac{1}{2}}\right] * \left[\begin{array}{c} 1 + K_1^{1/2}[H_2]^{\frac{1}{2}} + K_2[NO_2^-] + K_1^{1/2} K_2 K_3 [H_2]^{1/2} [NO_2^-][H^+] + \cdots \\ K_1 K_2 K_3 K_4 [H_2][NO_2^-][H^+] \end{array}\right]^2} \quad (8)$$

Overall, presence of water molecules does not change the reaction mechanism as the hydrogenation of NO* still follows the HNO path. However, there is a subtle but noticeable change of the relative difference between TS1 and TS2. That is, the second hydrogenation has either a larger (by 0.2 eV) or comparable apparent barrier, as compared to the first hydrogenation. This finding is in good agreement with our further kinetic fitting analysis.

Finally, we want to briefly discuss the selectivity to N_2 and NH_3 based on the DFT calculations. Fig. 3 suggests that the N-N coupling barriers between different surface species (N*, NO*, NH*. HNO*, HNOH*) are all higher than the corresponding hydrogenation barriers, indicating NH_3 formation to be more favorable. However, it should be noticed that NO* and its reaction intermediates bind stronger with Pd than hydrogen does. The prominence of the N_2 product observed in experiments could be due to the high coverage of NO* and its intermediates on the Pd surface, which leads to a competitive coupling reaction toward N_2 over the hydrogenation. This explains the high selectivity of the catalyst towards nitrogen (>98 %) for the different reaction conditions employed. This interpretation is in good agreement with the observation that at the end of a batch experiment, the Pd surface is almost completely covered with remarkably stable N atoms.[69].

3.3. Langmuir-Hinshelwood reaction kinetics

3.3.1. Rate expression development

As previously explained, the mechanism for nitrite hydrogenation involves barrierless formation of NO* on the palladium surface from chemisorbed NO_2^- and H_2, followed by sequential hydrogenation reactions to form HNO*, HNOH*, and HN*. As shown in the SI Section 6, the only possible mechanism that would lead to reaction orders for hydrogen that vary from 0 to 1.5, and thus fitting our results, is that involving co-limiting hydrogenation of NO* and HNO*. Choosing a single RDS would unavoidably lead to variations of the reaction orders for hydrogen that vary between 0 and 1 for NO* hydrogenation or 0.5–1.5 for HNO* hydrogenation, which would be inconsistent with experimentally measured values. In this scenario, the elementary steps are as follows:

1. $H_2 + 2* \leftrightharpoons 2H^*$ (dissociative hydrogen adsorption, $\boldsymbol{K}_1$)
2. $NO_2^- + * \rightleftharpoons NO_2^{-*}$ (molecular nitrite adsorption, $\boldsymbol{K}_2$)

If one considers that the concentration of the $[H^+]$ is low and constant (about 10^{-5} mol L^{-1}) in comparison to NO_2^- and H_2 concentrations (~10^{-3} mol L^{-1}), then it is possible to neglect the influence of protons in this buffered system. In this sense, the expression above can be simplified to Eq. (9).

$$r_{NO_2^-} = \frac{k_5 k_4 {K_1}^{3/2} K_2 K_3 [H_2]^{3/2} [NO_2^-]}{\left[k_{-4} + k_5 K_1^{1/2} [H_2]^{1/2}\right] * \left[1 + K_1^{1/2}[H_2]^{\frac{1}{2}} + K_2[NO_2^-]\right]^2} \quad (9)$$

In this rate expression (Eq. (9)), one can immediately recognize that the reaction order for hydrogen and nitrite vary from 0 to 1.5 and −1 to 1, respectively.

3.4. Kinetic fitting analysis

We employed the extensive kinetic data presented in Fig. 1 to evaluate the validity of the dual RDS mechanism. For this purpose, we used as input values for the error minimization algorithm the Gibbs free energies calculated by DFT for steps 4, −4, and 5. In this analysis, we limited our fitting to the regression of the equilibrium and reaction constants. Here, it is important to mention that the optimized values of the Gibbs free energies of adsorption and activation were close to those obtained from the DFT calculation, indicating that these optimized values are physically meaningful.

Here, we observed that the model involving step 6 as RDS leads to large residual error, AIC, and low correlation coefficient at low and high temperatures (see Table S1). In contrast, when the RDS is moved earlier in the mechanism to either steps 4 or 5 the goodness of the fitting improves. We observe that when the reaction temperature is 25 °C, step 4,5 both as RDS has the smallest residual error, AIC and high correlation coefficient, which means the best fitting is obtained. However, when the temperature increased to 25 °C, steps 4 as RDS lead to the smallest residual error, AIC and high correlation coefficient. Essentially, this analysis suggests that as the reaction conditions are varied the system is either controlled by step 4, 5 or both. The kinetic fitting of step 4,5 as RDS are show in Fig. S11.

3.5. Degree of rate control

We examined the degree of rate control of the step 4 and 5 over a large range of experimental conditions using the dual RDS model. We defined the Degree of Rate Control, X_{RC}, for elementary step, i, as described by Campbell (Eq. (10)). [79,80].

$$X_{RC,i} = \frac{k_i}{r}\left(\frac{\partial r}{\partial k_i}\right)_{k_{j\neq i},K_i} \quad (10)$$

In order to assess the influence of temperature on the X_{RC} we estimated the values of the heat and entropies of adsorption using the Van't Hoff equation for the equilibrium between the reactants in the liquid phase and the palladium surface, while the activation enthalpies and entropies were regressed using transition state treatments. To ensure thermodynamic consistency, we followed the criteria proposed by Vannice,[81] including; (1) heat of adsorption must be negative for adsorbing species, (2) there must be a decrease in entropy upon adsorption, and (3) the molecule cannot lose more entropy than it possesses before adsorption (see Section S7 and S8).

Our statistically optimal model predicts that, in general, both surface reactions are kinetically significant and the degree of rate control from each is sensitive to the operating conditions. As shown in Fig. 5a, at 25 °C the rate control lies primarily with step 5 at low hydrogen partial pressures (c.a. 0.01 bar), explaining the high reaction orders measured. Increasing the partial pressure of hydrogen above 0.1 bar drastically led to a shift in the X_{RC} to step 4, which is consistent with the low reaction orders of hydrogen experimentally observed. Likewise, increasing the temperature shifted the rate control from step 5 to step 4 (Fig. 5b) at low hydrogen partial pressure (0.01 bar). These results are in line with the slight decrease in the apparent reaction orders in hydrogen from 1.4 to 1.2 at 25 °C and 50 °C, respectively. Notably, at high hydrogen partial pressures (0.8 bar) the X_{RC} is dominated by step 4 of the reaction (Fig. 5c). This explains the low sensitivity of the reaction orders near the saturation regime. These results illustrate the key role of the surface coverage in the large variations of the reaction orders for hydrogen in hydrogenation reactions.

4. Conclusions

We have provided new experimental and theoretical insights into the reaction mechanism of nitrite hydrogenation on Pd catalysts that suggests that the large variations of the apparent reaction orders with the partial pressures of hydrogen, nitrite concentration, and temperature are correlated to a co-limiting rate limiting step.

Rigorous Density Functional Theory calculations shows that the hydrogenation of NO via the nitrogen adatom is kinetically favored HNO over the NOH pathway. Furthermore, when explicit water molecules are included in the model to actively participate in the reaction via proton shuttling the activation energy barriers are

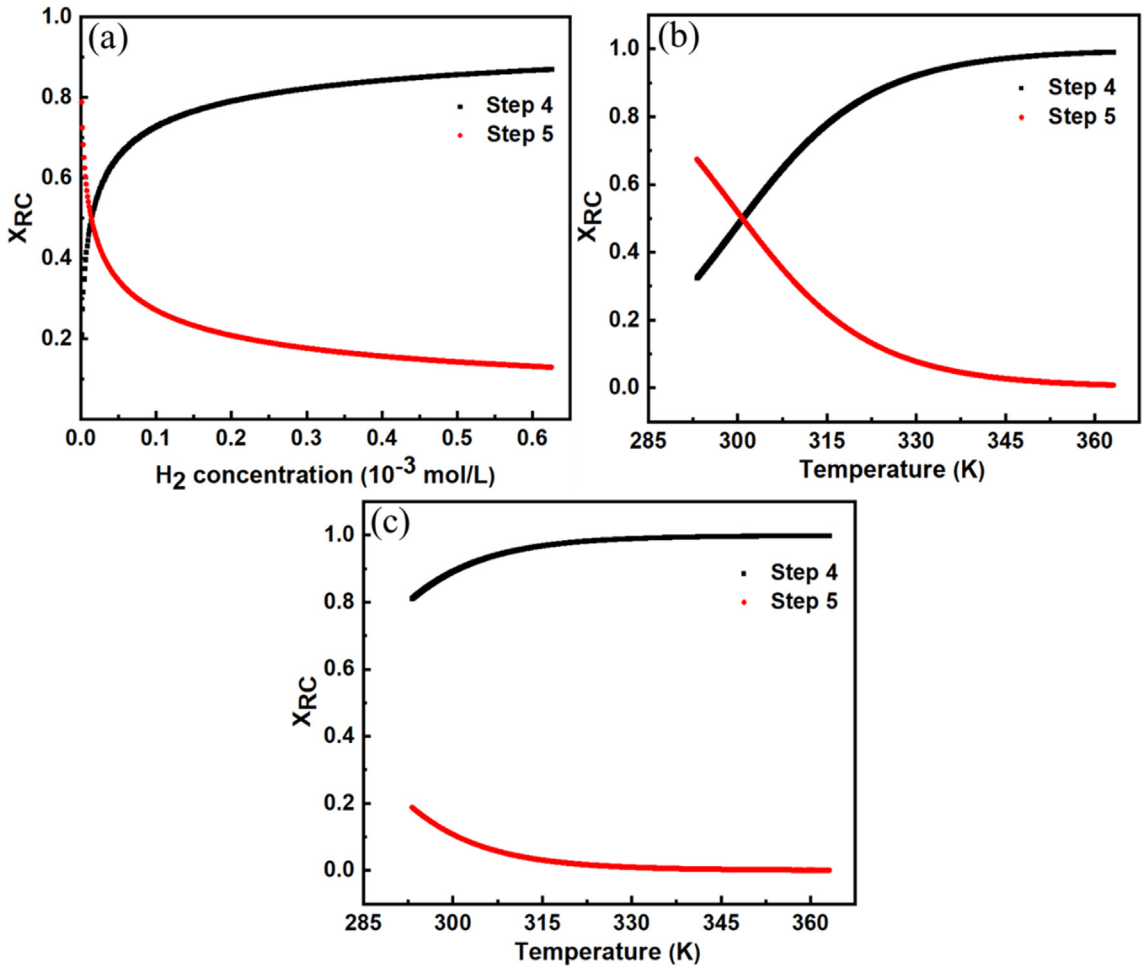

Fig. 5. Degree of Rate Control as a function of hydrogen pressure (a) at 25 °C. Degree of Rate Control as a function of temperature:(b) pH_2 = 0.01 bar, (c) pH_2 = 0.8 bar. Results were generated using the optimal parameter set from the kinetic fitting in section 3.4.

reduced in comparison to non-assisted hydrogenation using implicit solvent models. This flattening of the energy landscape is in line with the observed reaction kinetics, and kinetic isotope effect measurements that suggest that NO* and HNO* hydrogenation reactions are co-limiting this reaction. Finally, the interdependence of the surface coverages and the extent of kinetic control of these two steps is clearly showcased by the LH kinetic modelling and degree of rate control analysis. Our results, reveal the importance of considering both chemical potentials of reacting species (partial pressures and surface coverages) and the Gibbs free energies of activation (rate and adsorption constants) in analyzing the seemingly simple nitrite hydrogenation reaction on palladium.

Declaration of Competing Interest

The authors declare that they have no known competing financial interests or personal relationships that could have appeared to influence the work reported in this paper.

Acknowledgements

The authors gratefully acknowledge financial support from China Scholarship Council. (NO.201809505005) We are grateful to Rodrigo Fernández-Pacheco from Zaragoza University for the TEM analysis, K. Altena–Schildkamp for chemical analysis. B. Geerdink for technical support. The computations were performed at the OU Supercomputing Center for Education & Research and the National Energy Research Scientific Computing Center (NERSC), a U.S. Department of Energy Office of Science User Facility, and were supported by the U.S. Department of Energy, Basic Energy Sciences (Grant DE-SC0018284).

Data access

The data and models herein reported are accessible upon request to the corresponding authors.

Appendix A. Supplementary data

Supplementary data to this article can be found online at https://doi.org/10.1016/j.jcat.2022.06.007.

References

[1] W.G. Zumft, Cell biology and molecular basis of denitrification, Microbiol. Mol. Biol. Rev. 61 (4) (1997) 533–616, https://doi.org/10.1128/mmbr.61.4.533-616.1997.
[2] P.H. Debye, E. Zur, Theorie der Elektrolyte. I. Gefrierpunktserniedrigung und verwandte Erscheinungen, Phys. Zeitschrift. 24 (1923) 185–206, https://doi.org/10.1063/1.1724503.
[3] J.G. Kirkwood, Theory of solutions of molecules containing widely separated charges with special application to zwitterions, J. Chem. Phys. 2 (7) (1934) 351–361, https://doi.org/10.1063/1.1749489.
[4] M.J. Kamlet, J.L.M. Abboud, M.H. Abraham, R.W. Taft, linear solvation energy relationships. 23. A comprehensive collection of the solvatochromic parameters, π, α, and β, and some methods for simplifying the generalized solvatochromic equation, J. Org. Chem. 48 (1983) 2877–2887, https://doi.org/10.1021/jo00165a018.
[5] D.S. Potts, D.T. Bregante, J.S. Adams, C. Torres, D.W. Flaherty, Influence of solvent structure and hydrogen bonding on catalysis at solid–liquid interfaces, Chem. Soc. Rev. 50 (22) (2021) 12308–12337, https://doi.org/10.1039/D1CS00539A.
[6] G. Li, B. Wang, D.E. Resasco, Solvent effects on catalytic reactions and related phenomena at liquid-solid interfaces, Surf. Sci. Rep. 76 (4) (2021) 100541, https://doi.org/10.1016/j.surfrep.2021.100541.
[7] U. Prüsse, M. Hähnlein, J. Daum, K.-D. Vorlop, Improving the catalytic nitrate reduction, Catal. Today 55 (1-2) (2000) 79–90, https://doi.org/10.1016/S0920-5861(99)00228-X.
[8] K.N. Heck, S. Garcia-Segura, P. Westerhoff, M.S. Wong, Catalytic converters for water treatment, Acc. Chem. Res. 52 (4) (2019) 906–915, https://doi.org/10.1021/acs.accounts.8b00642.
[9] A. Kapoor, T. Viraraghavan, Nitrate removal from drinking water—review, J. Environ. Eng. 123 (4) (1997) 371–380, https://doi.org/10.1061/(ASCE)0733-9372(1997)123:4(371).
[10] D.E. Canfield, A.N. Glazer, P.G. Falkowski, The evolution and future of earth's nitrogen cycle, Science (80-) 330 (6001) (2010) 192–196, https://doi.org/10.1126/science.1186120.
[11] C.S. Bruning-Fann, J.B. Kaneene, The effects of nitrate, nitrite and N-nitroso compounds on human health: a review, Vet. Hum. Toxicol. 35 (6) (1993) 521–538.
[12] F. Edition, Guidelines for drinking-water quality, WHO Chron. 38 (2011) 104–108.
[13] S. Ebbesen, B. Mojet, L. Lefferts, In situ attenuated total reflection infrared (ATR-IR) study of the adsorption of NO, Langmuir 24 (3) (2008) 869–879, https://doi.org/10.1021/la7027725.
[14] A.J. Lecloux, Chemical, biological and physical constrains in catalytic reduction processes for purification of drinking water, Catal. Today 53 (1999) 23–34, https://doi.org/10.1016/S0920-5861(99)00100-5.
[15] M. Hu, Y. Liu, Z. Yao, L. Ma, X. Wang, Catalytic reduction for water treatment, Front. Environ. Sci. Eng. 12 (2018) 1–18, https://doi.org/10.1007/s11783-017-0972-0.
[16] V. Höller, I. Yuranov, L. Kiwi-Minsker, A. Renken, Structured multiphase reactors based on fibrous catalysts: Nitrite hydrogenation as a case study, Catal. Today 69 (1-4) (2001) 175–181, https://doi.org/10.1016/S0920-5861(01)00367-4.
[17] A. Obuchi, S. Naito, T. Onishi, K. Tamaru, Mechanism of catalytic reduction of NO by H2 or CO on a Pd foil; Role of chemisorbed nitrogen on Pd, Surf. Sci. 122 (2) (1982) 235–255, https://doi.org/10.1016/0039-6028(82)90076-0.
[18] S. Hörold, K.-D. Vorlop, T. Tacke, M. Sell, Development of catalysts for a selective nitrate and nitrite removal from drinking water, Catal. Today 17 (1-2) (1993) 21–30, https://doi.org/10.1016/0920-5861(93)80004-K.
[19] V. Matějů, S. Čižinská, J. Krejčí, T. Janoch, Biological water denitrification-a review, Enzyme Microb. Technol. 14 (3) (1992) 170–183, https://doi.org/10.1016/0141-0229(92)90062-S.
[20] K.T. Ranjit, B. Viswanathan, Photocatalytic reduction of nitrite and nitrate ions to ammonia on M/TiO2 catalysts, J. Photochem. Photobiol. A Chem. 108 (1) (1997) 73–78, https://doi.org/10.1016/S1010-6030(96)04505-4.
[21] H.C. Aran, J.K. Chinthaginjala, R. Groote, T. Roelofs, L. Lefferts, M. Wessling, R.G. H. Lammertink, Porous ceramic mesoreactors: a new approach for gas-liquid contacting in multiphase microreaction technology, Chem. Eng. J. 169 (1-3) (2011) 239–246, https://doi.org/10.1016/j.cej.2010.11.005.
[22] C.A. Clark, C.P. Reddy, H. Xu, K.N. Heck, G. Luo, T.P. Senftle, M.S. Wong, Mechanistic insights into pH-controlled nitrite reduction to ammonia and hydrazine over rhodium, ACS Catal. 10 (1) (2020) 494–509, https://doi.org/10.1021/acscatal.9b03239.
[23] P. Xu, S. Agarwal, L. Lefferts, Mechanism of nitrite hydrogenation over Pd/γ-Al2O3 according a rigorous kinetic study, J. Catal. 383 (2020) 124–134, https://doi.org/10.1016/j.jcat.2020.01.003.
[24] Z. Zhang, W. Shi, W. Wang, Y. Xu, X. Bao, R. Zhang, B. Zhang, Y. Guo, F. Cui, Interfacial electronic effects of palladium nanocatalysts on the by-product ammonia selectivity during nitrite catalytic reduction, Environ. Sci, NANO 5 (2) (2018) 338–349, https://doi.org/10.1039/C7EN00909G.
[25] O.M. Ilinitch, L.V. Nosova, V.V. Gorodetskii, V.P. Ivanov, S.N. Trukhan, E.N. Gribov, S.V. Bogdanov, F.P. Cuperus, Catalytic reduction of nitrate and nitrite ions by hydrogen: investigation of the reaction mechanism over Pd and Pd–Cu catalysts, J. Mol. Catal. A Chem. 158 (1) (2000) 237–249, https://doi.org/10.1016/S1381-1169(00)00070-4.
[26] I. Mikami, Y. Sakamoto, Y. Yoshinaga, T. Okuhara, Kinetic and adsorption studies on the hydrogenation of nitrate and nitrite in water using Pd-Cu on active carbon support, Appl. Catal. B Environ. 44 (1) (2003) 79–86, https://doi.org/10.1016/S0926-3373(03)00021-3.
[27] J. Wärn«, I. Turunen, T. Salmi, T. Maunula, Kinetics of nitrate reduction in monolith reactor, Chem. Eng. Sci. 49 (24) (1994) 5763–5773, https://doi.org/10.1016/0009-2509(94)00331-9.
[28] M. Duca, B. van der Klugt, M.A. Hasnat, M. Machida, M.T.M. Koper, Electrocatalytic reduction of nitrite on a polycrystalline rhodium electrode, J. Catal. 275 (1) (2010) 61–69, https://doi.org/10.1016/j.jcat.2010.07.013.
[29] H. Shin, S. Jung, S. Bae, W. Lee, H. Kim, Nitrite reduction mechanism on a Pd surface, Environ. Sci. Technol. 48 (21) (2014) 12768–12774, https://doi.org/10.1021/es503772x.
[30] A. Pintar, G. Berčič, J. Levec, Catalytic liquid-phase nitrite reduction: Kinetics and catalyst deactivation, AIChE J. 44 (1998) 2280–2292, https://doi.org/10.1002/aic.690441017.
[31] M.J.E. da Silva, L. Lefferts, J.A. Faria Albanese, N-isopropylacrylamide polymer brushes alter the micro-solvation environment during aqueous nitrite hydrogenation on Pd/Al_2O_3 catalyst, J. Catal. 402 (2021) 114–124, https://doi.org/10.1016/j.jcat.2021.08.003.
[32] J. Sa, T. Berger, K. Fottinger, A. Riss, J. Anderson, H. Vinek, Can TiO_2 promote the reduction of nitrates in water?, J. Catal. 234 (2) (2005) 282–291, https://doi.org/10.1016/j.jcat.2005.06.015.
[33] S.D. Ebbesen, B.L. Mojet, L. Lefferts, In situ attenuated total reflection infrared (ATR-IR) study of the adsorption of NO_2^-, NH_2OH, and NH_4^+ on Pd/Al_2O_3 and Pt/Al_2O_3, Langmuir 24 (3) (2008) 869–879, https://doi.org/10.1021/la7027725.
[34] S. Ebbesen, B. Mojet, L. Lefferts, In situ ATR-IR study of nitrite hydrogenation over Pd/Al_2O_3, J. Catal. 256 (1) (2008) 15–23, https://doi.org/10.1016/j.jcat.2008.02.013.

[35] L.Y. Huai, C.Z. He, H. Wang, H. Wen, W.C. Yi, J.Y. Liu, NO dissociation and reduction by H2 on Pd(111): a first-principles study, J. Catal. 322 (2015) 73–83, https://doi.org/10.1016/j.jcat.2014.11.011.
[36] S. Guo, K. Heck, S. Kasiraju, H. Qian, Z. Zhao, L.C. Grabow, J.T. Miller, M.S. Wong, Insights into nitrate reduction over indium-decorated palladium nanoparticle catalysts, ACS Catal. 8 (1) (2018) 503–515, https://doi.org/10.1021/acscatal.7b01371.
[37] Z. Zhao, R. Bababrik, W. Xue, Y. Li, N.M. Briggs, D.-T. Nguyen, U. Nguyen, S.P. Crossley, S. Wang, B. Wang, D.E. Resasco, Solvent-mediated charge separation drives alternative hydrogenation path of furanics in liquid water, Nat. Catal. 2 (5) (2019) 431–436, https://doi.org/10.1038/s41929-019-0257-z.
[38] M.A. Mellmer, C. Sanpitakseree, B. Demir, P. Bai, K. Ma, M. Neurock, J.A. Dumesic, Solvent-enabled control of reactivity for liquid-phase reactions of biomass-derived compounds, Nat. Catal. 1 (3) (2018) 199–207, https://doi.org/10.1038/s41929-018-0027-3.
[39] A.K. Chew, T.W. Walker, Z. Shen, B. Demir, L. Witteman, J. Euclide, G.W. Huber, J.A. Dumesic, R.C. Van Lehn, Effect of mixed-solvent environments on the selectivity of acid-catalyzed dehydration reactions, ACS Catal. 10 (3) (2020) 1679–1691, https://doi.org/10.1021/acscatal.9b03460.
[40] D.T. Bregante, A.M. Johnson, A.Y. Patel, E.Z. Ayla, M.J. Cordon, B.C. Bukowski, J. Greeley, R. Gounder, D.W. Flaherty, Cooperative effects between hydrophilic pores and solvents: catalytic consequences of hydrogen bonding on alkene epoxidation in zeolites, J. Am. Chem. Soc. 141 (18) (2019) 7302–7319, https://doi.org/10.1021/jacs.8b12861.
[41] J. Wang, S. Zeng, N. Chen, D. Shang, X. Zhang, J. Li, Research progress of ammonia adsorption materials, Guocheng Gongcheng Xuebao/The Chinese, J. Process Eng. 19 (2019) 14–24, https://doi.org/10.12034/j.issn.1009-606X.218171.
[42] G. Li, B. Wang, T. Kobayashi, M. Pruski, D.E. Resasco, Optimizing the surface distribution of acid sites for cooperative catalysis in condensation reactions promoted by water, Chem Catal. 1 (5) (2021) 1065–1087, https://doi.org/10.1016/j.checat.2021.08.005.
[43] J.S. Bates, B.C. Bukowski, J. Greeley, R. Gounder, Structure and solvation of confined water and water-ethanol clusters within microporous Brønsted acids and their effects on ethanol dehydration catalysis, Chem. Sci. 11 (27) (2020) 7102–7122, https://doi.org/10.1039/D0SC02589E.
[44] J.K. Chinthaginjala, L. Lefferts, Support effect on selectivity of nitrite reduction in water, Appl. Catal. B Environ. 101 (1-2) (2010) 144–149, https://doi.org/10.1016/j.apcatb.2010.09.023.
[45] R. Brunet Espinosa, D. Rafieian, R.S. Postma, R.G.H. Lammertink, L. Lefferts, Egg-shell membrane reactors for nitrite hydrogenation: Manipulating kinetics and selectivity, Appl. Catal. B Environ. 224 (2018) 276–282, https://doi.org/10.1016/j.apcatb.2017.10.058.
[46] Y. Matatov-Meytal, Y. Shindler, M. Sheintuch, Cloth catalysts in water denitrification: III. pH inhibition of nitrite hydrogenation over Pd/ACC, Appl. Catal. B Environ. 45 (2) (2003) 127–134, https://doi.org/10.1016/S0926-3373(03)00126-7.
[47] W. Stöber, A. Fink, E. Bohn, Controlled growth of monodisperse silica spheres in the micron size range, J. Colloid Interface Sci. 26 (1) (1968) 62–69, https://doi.org/10.1016/0021-9797(68)90272-5.
[48] X. Hao, S. Barnes, J.R. Regalbuto, A fundamental study of Pt impregnation of carbon: adsorption equilibrium and particle synthesis, J. Catal. 279 (1) (2011) 48–65, https://doi.org/10.1016/j.jcat.2010.12.021.
[49] M.-g. Seo, D.-W. Lee, S.S. Han, K.-Y. Lee, Direct synthesis of hydrogen peroxide from hydrogen and oxygen over mesoporous silica-shell-coated, palladium-nanocrystal-grafted SiO2 nanobeads, ACS Catal. 7 (4) (2017) 3039–3048, https://doi.org/10.1021/acscatal.7b00388.
[50] R.A. Vargas−Hernández, Bayesian optimization for calibrating and selecting hybrid-density functional models, J. Phys. Chem. A. 124 (20) (2020) 4053–4061, https://doi.org/10.1021/acs.jpca.0c01375.
[51] G. Kresse, J. Furthmüller, Efficiency of ab-initio total energy calculations for metals and semiconductors using a plane-wave basis set, Comput. Mater. Sci. 6 (1) (1996) 15–50, https://doi.org/10.1016/0927-0256(96)00008-0.
[52] G. Kresse, J. Hafner, Ab initio molecular-dynamics simulation of the liquid-metal–amorphous-semiconductor transition in germanium, Phys. Rev. B. 49 (1994) 14251, https://doi.org/10.1103/PhysRevB.49.14251.
[53] P.E. Blöchl, Projector augmented-wave method, Phys. Rev. B. 50 (24) (1994) 17953–17979, https://doi.org/10.1103/PhysRevB.50.17953.
[54] G. Kresse, D. Joubert, From ultrasoft pseudopotentials to the projector augmented-wave method, Phys. Rev. B. 59 (1999) 1758, https://doi.org/10.1103/PhysRevB.59.1758.
[55] S. Grimme, J. Antony, S. Ehrlich, H. Krieg, A consistent and accurate ab initio parametrization of density functional dispersion correction (DFT-D) for the 94 elements H-Pu, J. Chem. Phys. 132 (2010) 154104, https://doi.org/10.1063/1.3382344.
[56] M. Chen, Y. Yan, M. Gebre, C. Ordonez, F. Liu, L. Qi, A. Lamkins, D. Jing, K. Dolge, B. Zhang, P. Heintz, D.P. Shoemaker, B. Wang, W. Huang, Thermal unequilibrium of PdSn intermetallic nanocatalysts: from in situ tailored synthesis to unexpected hydrogenation selectivity, Angew. Chemie Int. Ed. 60 (2021) 18309–18317, doi: 10.1002/anie.202106515.
[57] K. Mathew, R. Sundararaman, K. Letchworth-Weaver, T.A. Arias, R.G. Hennig, Implicit solvation model for density-functional study of nanocrystal surfaces and reaction pathways, J. Chem. Phys. 140 (2014) 1–8, https://doi.org/10.1063/1.4865107.
[58] A. Heyden, A.T. Bell, F.J. Keil, Efficient methods for finding transition states in chemical reactions: comparison of improved dimer method and partitioned rational function optimization method, J. Chem. Phys. 123 (2005) 224101.
[59] G. Henkelman, B.P. Uberuaga, H. Jónsson, A climbing image nudged elastic band method for finding saddle points and minimum energy paths, J. Chem. Phys. 113 (22) (2000) 9901–9904, https://doi.org/10.1063/1.1329672.
[60] M. Yamauchi, R. Ikeda, H. Kitagawa, M. Takata, Nanosize effects on hydrogen storage in palladium, J. Phys. Chem. C. 112 (9) (2008) 3294–3299, https://doi.org/10.1021/jp710447j.
[61] X. Gao, A. Heyden, O.A. Abdelrahman, J.Q. Bond, Microkinetic analysis of acetone hydrogenation over Pt/SiO_2, J. Catal. 374 (2019) 183–198, https://doi.org/10.1016/j.jcat.2019.04.033.
[62] H. Akaike, A new look at the statistical model identification, IEEE Trans. Automat. Contr. 19 (6) (1974) 716–723, https://doi.org/10.1109/TAC.1974.1100705.
[63] V. Höller, K. Rådevik, I. Yuranov, L. Kiwi-Minsker, A. Renken, Reduction of nitrite-ions in water over Pd-supported on structured fibrous materials, Appl. Catal. B Environ. 32 (3) (2001) 143–150, https://doi.org/10.1016/S0926-3373(01)00139-4.
[64] V. Rosca, M. Duca, M.T. de Groot, M.T.M. Koper, Nitrogen cycle electrocatalysis, Chem. Rev. 109 (6) (2009) 2209–2244, https://doi.org/10.1021/cr8003696.
[65] J. Bigeleisen, M. Wolfsberg, Isotope Effects in Chemical Kinetics, Advances in Chemical Physics 1 (1958).
[66] K.B. Wiberg, The deuterium isotope effect, Chem. Rev. 55 (4) (1955) 713–743.
[67] S.D. Ebbesen, B.L. Mojet, L. Lefferts, Mechanistic investigation of the heterogeneous hydrogenation of nitrite over Pt/Al_2O_3 by attenuated total reflection infrared spectroscopy, J. Phys. Chem. C. 113 (6) (2009) 2503–2511, https://doi.org/10.1021/jp8081886.
[68] R. Zhang, D. Shuai, K.A. Guy, J.R. Shapley, T.J. Strathmann, C.J. Werth, Elucidation of nitrate reduction mechanisms on a Pd-in bimetallic catalyst using isotope labeled nitrogen species, ChemCatChem 5 (1) (2013) 313–321, https://doi.org/10.1002/cctc.201200457.
[69] Y. Zhao, N. Koteswara Rao, L. Lefferts, Adsorbed species on Pd catalyst during nitrite hydrogenation approaching complete conversion, J. Catal. 337 (2016) 102–110, https://doi.org/10.1016/j.jcat.2016.02.007.
[70] C.P. Theologides, G.G. Olympiou, P.G. Savva, K. Kapnisis, A. Anayiotos, C.N. Costa, Mechanistic aspects (SSITKA-DRIFTS) of the catalytic denitrification of water with hydrogen on Pd-Cu supported catalysts, Appl. Catal. B Environ. 205 (2017) 443–454, https://doi.org/10.1016/j.apcatb.2016.12.055.
[71] X. Huo, D.J. Van Hoomissen, J. Liu, S. Vyas, T.J. Strathmann, Hydrogenation of aqueous nitrate and nitrite with ruthenium catalysts, Appl. Catal. B Environ. 211 (2017) 188–198, https://doi.org/10.1016/j.apcatb.2017.04.045.
[72] S.D. Ebbesen, B.L. Mojet, L. Lefferts, Effect of pH on the nitrite hydrogenation mechanism over Pd/Al_2O_3 and Pt/Al_2O_3: details obtained with ATR-IR spectroscopy, J. Phys. Chem. C. 115 (4) (2011) 1186–1194, https://doi.org/10.1021/jp106521t.
[73] Y.B. Yin, S. Guo, K.N. Heck, C.A. Clark, C.L. Conrad, M.S. Wong, Treating water by degrading oxyanions using metallic nanostructures, ACS Sustain. Chem. Eng. 6 (9) (2018) 11160–11175, https://doi.org/10.1021/acssuschemeng.8b02070.
[74] X. Fan, C. Franch, E. Palomares, A.A. Lapkin, Simulation of catalytic reduction of nitrates based on a mechanistic model, Chem. Eng. J. 175 (2011) 458–467, https://doi.org/10.1016/j.cej.2011.09.069.
[75] D.T. Bregante, M.C. Chan, J.Z. Tan, E.Z. Ayla, C.P. Nicholas, D. Shukla, D.W. Flaherty, The shape of water in zeolites and its impact on epoxidation catalysis, Nat. Catal. 4 (9) (2021) 797–808, https://doi.org/10.1038/s41929-021-00672-4.
[76] K.A.T. Silverstein, A.D.J. Haymet, K.A. Dill, The strength of hydrogen bonds in liquid water and around nonpolar solutes, J. Am. Chem. Soc. 122 (33) (2000) 8037–8041.
[77] G.E. Walrafen, Y.C. Chu, Shear viscosity, heat capacity, and fluctuations of liquid water, all at constant molal volume, J. Phys. Chem. 95 (22) (1991) 8909–8921.
[78] B.R. Goldsmith, T. Hwang, S. Seritan, B. Peters, S.L. Scott, Rate-enhancing roles of water molecules in methyltrioxorhenium-catalyzed olefin epoxidation by hydrogen peroxide, J. Am. Chem. Soc. 137 (30) (2015) 9604–9616.
[79] C.T. Campbell, The degree of rate control: a powerful tool for catalysis research, ACS Catal. 7 (4) (2017) 2770–2779, https://doi.org/10.1021/acscatal.7b00115.
[80] Z. Mao, C.T. Campbell, The degree of rate control of catalyst-bound intermediates in catalytic reaction mechanisms: Relationship to site coverage, J. Catal. 381 (2020) 53–62, https://doi.org/10.1016/j.jcat.2019.09.044.
[81] M.S. Spencer, Kinetics of catalytic reactions, Appl. Catal. 44 (1988) 274–275, https://doi.org/10.1016/S0166-9834(00)80062-7.